Chemistry–A European Journal
Research Article
doi.org/10.1002/chem.202201784
Chemistry Europe
European Chemical Societies Publishing
www.chemeurj.org

Improving the Electrocatalytic Activity of a Nickel-Organic Framework toward the Oxygen Evolution Reaction through Vanadium Doping

Hongbo Yu[+],[a] Lixia Wang[+],[a] Huatong Li,[a] Zuyang Luo,[a] Tayirjan Taylor Isimjan,*[b] and Xiulin Yang*[a]

Abstract: Metal-organic frameworks (MOFs) have been considered as potential oxygen evolution reaction (OER) electrocatalysts owning to their ultra-thin structure, adjustable composition, high surface area, and high porosity. Here, we designed and fabricated a vanadium-doped nickel organic framework (V_{1-x}–Ni_xMOF) system by using a facile two-step solvothermal method on nickel foam (NF). The doping of vanadium remarkably elevates the OER activity of V_{1-x}–Ni_xMOF, thus demonstrating better performance than the corresponding single metallic Ni-MOF, NiV-MOF and RuO_2 catalysts at high current density ($>400\ mA\,cm^{-2}$). $V_{0.09}$–$Ni_{0.91}$MOF/NF provides a low overpotential of 235 mV and a small Tafel slope of $30.3\ mV\,dec^{-1}$ at a current density of $10\ mA\,cm^{-2}$. More importantly, a water-splitting device assembled with Pt/C/NF and $V_{0.09}$–$Ni_{0.91}$MOF/NF as cathode and anode yielded a cell voltage of 1.96 V@1000 $mA\,cm^{-2}$, thereby outperforming the-state-of-the-art $RuO_2^{(+)}||Pt/C^{(-)}$. Our work sheds new insight on preparing stable, efficient OER electrocatalysts and a promising method for designing various MOF-based materials.

Introduction

As fossil fuels are consumed at an ever-increasing rate and human demand for energy continues to increase, the development of sustainable energy sources becomes more urgent and important.[1] Overall electrochemical water splitting is considered to be an environmentally friendly and economically feasible alternative to produce clean chemical fuels with no carbon emissions, such as H_2 ($2H^+ + 2e^- \rightarrow H_2$) and O_2 ($4OH^- \rightarrow O_2 + 2H_2O$).[2] OER exhibits slow kinetics due to its four-electron transfer process, which requires an efficient electrocatalyst to lower the potential barrier.[3] Noble metal-based catalysts have been recognized as the most widely used advanced materials for OER, such as Ru-/Ir-based materials.[4] However, its low abundance and high cost limit the practical large-scale application.[5] Therefore, the preparation of abundant, inexpensive, and efficient non-noble-metal alternative electrocatalysts to improve the OER has become an urgent need in the current research field.[6]

Currently, a series of transition metal-based catalysts have been explored for efficient electrocatalytic oxygen evolution. Metal-organic frameworks (MOF) have attracted wide attention in the field of catalysis because of their unique advantages such as adjustable composition, high specific surface area and large pore structure.[7] However, the conductivity of most MOFs is relatively poor, which limits the overall conversion efficiency in chemical energy and long-term performance. Compared with monometallic MOF systems, most bimetallic MOFs generally exhibit enhanced OER activity, which is attributed to the tunable metal junction engineering and synergistic effects between different metals.[8] For instance, Ge et al. prepared a series of two-dimensional bimetallic MOF–Fe/Co nanosheet materials. The optimal catalyst reached $10\ mA\,cm^{-2}$ with only an overpotential of 238 mV in alkaline solution.[9] Additionally, the bimetallic Co_2Ni-MOF prepared by Zhou et al. exhibited distinguished OER performance with an overpotential of 240 mV at $10\ mA\,cm^{-2}$.[10] Shi et al. reported a tannin–NiFe (TANF) complex film on carbon fiber paper as an efficient OER electrocatalyst with a low Tafel slope of $28\ mV\,dec^{-1}$.[11] Moreover, modifying the surface electrical structure of MOFs by metal element doping has been proven in recent studies to be one of the most effective approaches to improve their intrinsic OER performance and stability.[12] Vanadium has been explored as an effective dopant due to its abundant valence state, which provides excellent feasibility for adjusting electronic structure and inducing synergistic interaction between dopant and host metal, thus improving the performance of OER effectively.[13] It was reported that V doping leads to a large number of free carriers around the Fermi level, which helps to improve the

[a] H. Yu,[+] L. Wang,[+] H. Li, Z. Luo, Prof. Dr. X. Yang
Guangxi Key Laboratory of Low Carbon Energy Materials
School of Chemistry and Pharmaceutical Sciences
Guangxi Normal University
Guilin 541004 (P. R. China)
E-mail: xlyang@gxnu.edu.cn

[b] Dr. T. T. Isimjan
Saudi Arabia Basic Industries Corporation (SABIC) at
King Abdullah University of Science and Technology (KAUST)
Thuwal 23955-6900 (Saudi Arabia)
E-mail: isimjant@sabic.com

[+] These authors contributed equally to this work.

Supporting information for this article is available on the WWW under https://doi.org/10.1002/chem.202201784

charge transfer efficiency of V-doped catalysts, thereby improving the electrochemical performance.[10] Moreover, Duan et al. synthesized V-doped NiCoP nanowires that exhibited outstanding OER performance in 1 M KOH with an overpotential of 254 mV at 10 mA cm^{-2}.[13a]

With the considerations mentioned above in mind, we designed a two-step solvothermal method to synthesize V_{1-x}–Ni_xMOF. The as-prepared $V_{0.09}$–$Ni_{0.91}$MOF/NF composite has the best oxygen evolution performance compared with a series of prepared catalysts, which required 235 mV (vs. RHE, Figure S1 in the Supporting Information) of overpotential to provide a current density of 10 mA cm^{-2}. As expected, the two-electrode system consisting of Pt/C/NF and $V_{0.09}$–$Ni_{0.91}$MOF/NF recorded a small cell voltage of 1.96 V at 1000 mA cm^{-2} in the water splitting test under alkaline conditions. This flexible preparation strategy and high-efficiency electrochemical oxygen evolution performance provide a promising direction and potential application for the development of MOFs-based electrocatalysts.

Results and Discussion

As illustrated in Scheme 1, the synthesis of $V_{0.09}$–$Ni_{0.91}$MOF/NF is primarily a two-step hydrothermal method. In the first stage, urea was employed to create an alkaline environment, and NH_4F was used as a structure-oriented growth agent to prepare Ni–V hydroxide in situ on the surface of NF. Then, the $V_{0.09}$–$Ni_{0.91}$MOF/NF material was reconstructed by Ni–V-OH/NF substrate in hydrothermal environment with the salt solution of Ni and V as the metal center and DHTA as the ligand. The atomic-level dispersion is realized due to the bifunctional ligand.

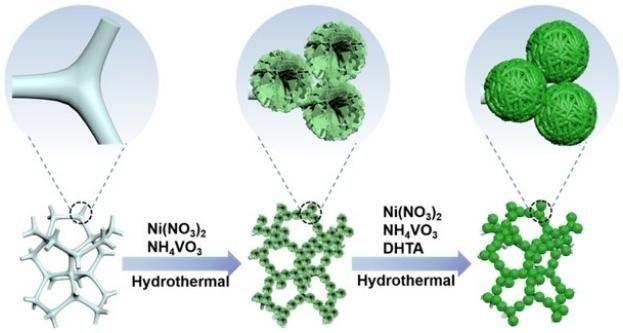

Scheme 1. Schematic illustration of the synthesis of $V_{0.09}$–$Ni_{0.91}$MOF/NF.

X-ray diffraction (XRD) has studied the phase structure of as-prepared V_{1-x}–Ni_xMOF catalysts. The composite on the NF surface was ultrasonically scraped off to avoid interference from the strong Ni diffraction peaks. The diffraction peaks of Ni–V hydroxide are composed of $Ni(OH)_2$ (JCPDS: 14-0117), $Ni(OH)_2 \cdot 0.75\,H_2O$ (JCPDS: 38-0715)[14] and $V_2O_2(OH)_3$ (JCPDS: 12-1380) as depicted in Figure 1a. After the second hydrothermal treatment, the diffraction peaks of the constructed Ni-MOF are in good alignment with the theoretically simulated Ni-MOF (Figure 1b). In the as-synthesized Ni-MOF structure, Ni^{2+} coordinates with the five carboxylic acid groups of the ligands to form a network structure of hexagonal channels (Figure S2). After introduction the V, the diffraction peaks of the prepared $V_{0.09}$–$Ni_{0.91}$MOF hybrid material are substantially identical to that of the Ni-MOF, possibly due to the low V content or the existence of amorphous form. Notably, the peak of $V_{0.09}$–$Ni_{0.91}$MOF showed a slightly positive shift (Figure 1c), indicating that V has been successfully doped into Ni-MOF.[15]

Scanning electron microscopy (SEM) images are used to investigate the microscopic morphologies of the produced samples. As seen in Figure 2a, the naked NF is a three-dimensional porous structure with relatively flat surface. After the hydrothermal reaction, flower-like NiV-OH grew on the NF surface (Figure 2b). After further solvothermal treatment, the flower-shaped composite transformed into a spherical structure (Figure 2c) and then converted to a spherical V-doped Ni-MOF on NiV-OH surface upon the addition of the DHTA. Furthermore, the three-dimensional open spherical framework can provide increased active area and improve mass transfer.[8b,16] Transmission electron microscopy (TEM) images of the ultrasonically exfoliated catalyst fragments showed that the $V_{0.09}$–$Ni_{0.91}$MOF surface was flake-like (Figure 2d), and some nanoparticles with an average size of about 0.89 nm (inset 2e) were uniformly distributed on its surface (Figure 2e). Selected area electron diffraction (SAED) in Figure 2f manifested that it was relatively weak crystallinity. Furthermore, the high annular dark-field scanning TEM (HAADF-STEM) image and the corresponding

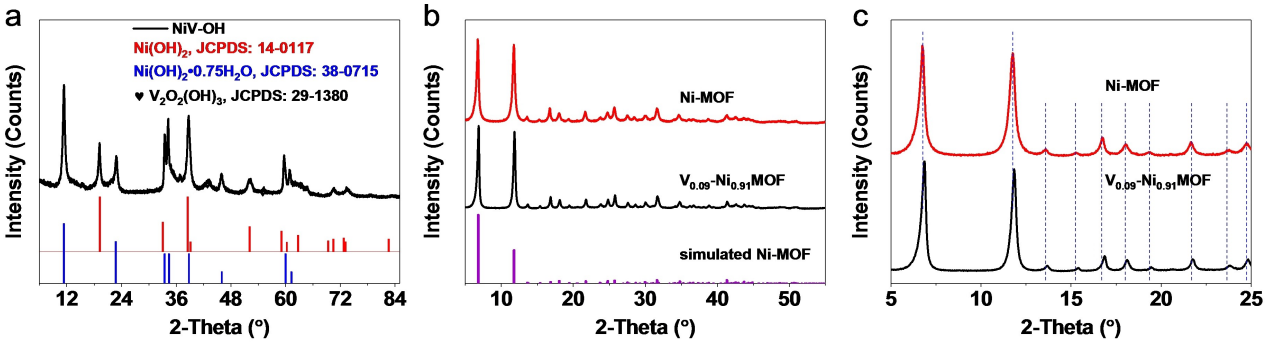

Figure 1. XRD patterns of a) NiV-OH, b) Ni-MOF, $V_{0.09}$–$Ni_{0.91}$MOF plus simulated Ni-MOF, and c) narrow-range XRD of Ni-MOF and $V_{0.09}$–$Ni_{0.91}$MOF.

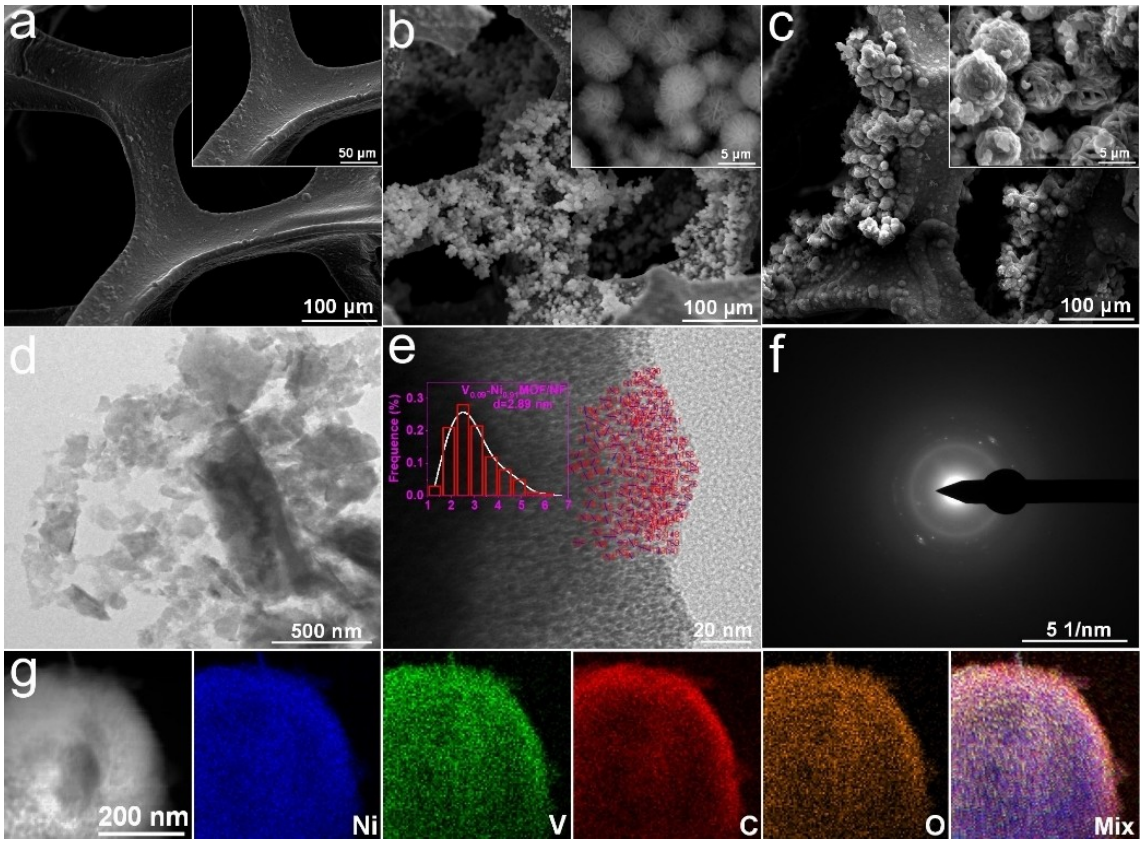

Figure 2. SEM images with (inset) high-magnification SEM images of a) bare NF, b) NiV-OH/NF, and c) $V_{0.09}$–$Ni_{0.91}$MOF/NF. d) TEM image, e) high-resolution TEM image with (inset) distribution of particle size diameter, f) SAED image, and g) HAADF-STEM image and the corresponding element mappings of $V_{0.09}$–$Ni_{0.91}$MOF/NF.

element mappings demonstrated that the elements of Ni, V, C and O are uniformly dispersed throughout the spherical structure of $V_{0.09}$–$Ni_{0.91}$MOF (Figure 2g).

Additionally, Fourier transform infrared spectroscopy was carried out to detect V-doped MOF composite, as shown in Figure 3a. And for comparison, the FTIR spectrum of pure DHTA was also investigated. The results show that the infrared spectrum of $V_{0.09}$–$Ni_{0.91}$MOF/NF is significantly different from that of the ligand DHTA. A large extent decreased the peak intensity of the undissociated hydroxyl band of the ligand, and the apparent shift of the carboxylic group from 1653 to 1558 cm^{-1} wavenumber in $V_{0.09}$–$Ni_{0.91}$MOF/NF, indicating the high degree of binding of the metal ions with the carboxylic acid functional groups. Others also observed similar phenomena.[17] As displayed in Figure 3b, the two composites also exhibit identical Raman spectra. The stretching and deformation vibrations of a benzene ring are represented by the Raman peaks at 1631 and 580 cm^{-1}, respectively. The ν(COO-) vibration is located at 1497 cm^{-1}. ν(C–O) arises at 1285 cm^{-1} due to the deprotonation of the hydroxy group after coordination, The C–H bending mode of the benzene ring and the metal-oxygen bond vibration have peaks at 832 and 415 cm^{-1}, respectively. The peaks at 832 and 415 cm^{-1} correspond to the C–H bending mode of the benzene ring and the metal-oxygen bond vibration, respectively.[18] The thermal decomposition of the $V_{0.09}$–$Ni_{0.91}$MOF in the air is shown in Figure 3c. The TGA and DTG show three prominent weight-loss stages where stage one indicates removing the water (~17.3%) from ligand detachment and adsorbed water molecules. The second step occurs at about 330 °C, with a weight loss of approximately 11.7%. The ligand begins to break off at this stage, and $V_{0.09}$–$Ni_{0.91}$MOF decomposes. The third step takes place at 430 °C with a weight-loss of ~33.0% caused by the carbonization and decomposition of the compound at high temperatures. Figure 3d depicts the N_2 adsorption and desorption isotherms of the samples. The specific surface area of $V_{0.09}$–$Ni_{0.91}$MOF is 885.4 $m^2 g^{-1}$, more prominent than that of Ni-MOF (875.0 $m^2 g^{-1}$) and Ni-OH (77.1 $m^2 g^{-1}$), which is beneficial to the catalytic active site exposure and mass transfer ability. Generally, the specific surface area of the catalyst is highly dependent on the particle size, pore size, and thickness of the nanosheet. Since the MOF material has a pore size distribution in the region of 2–50 nm, it exhibits mesoporous characteristics. The inset of Figure 3d is the pore size distribution curve, the average pore size of $V_{0.09}$–$Ni_{0.91}$MOF and Ni-MOF is close to 2.5 nm, whereas that of NiV-OH is about 8.5 nm. Although the pore sizes of $V_{0.09}$–$Ni_{0.91}$MOF and Ni-MOF are very similar, the particle size and thickness of the nanosheets played a crucial role in their specific surface area. The SEM and TEM images revealed that $V_{0.09}$–$Ni_{0.91}$MOF is a thin nanosheet composed of

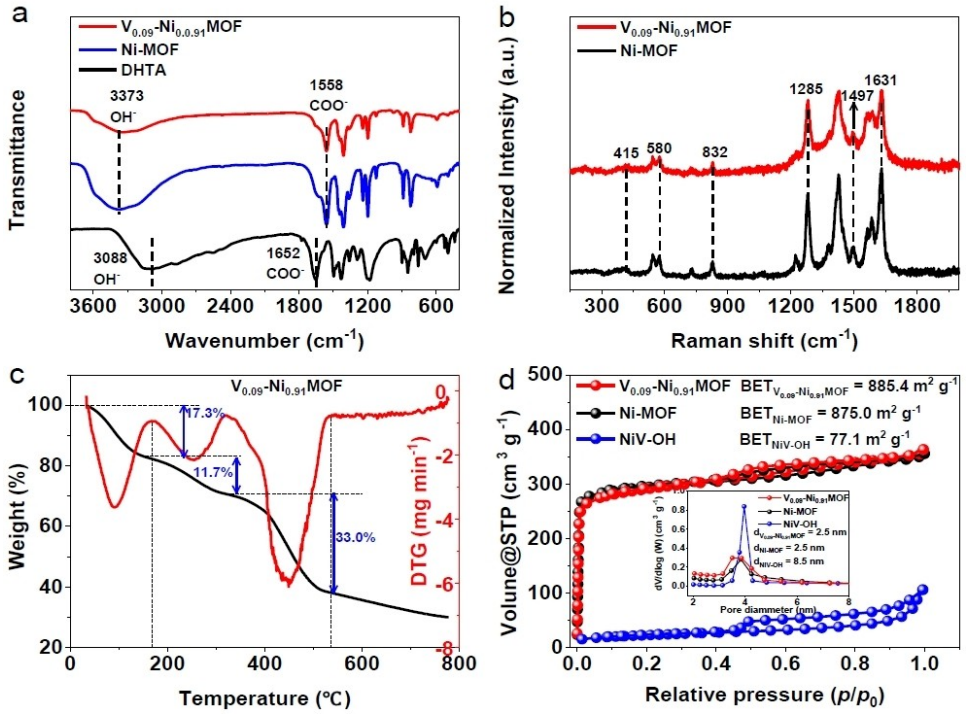

Figure 3. a) FTIR spectra of $V_{0.09}$–$Ni_{0.91}$MOF, Ni-MOF, and the DHTA ligand. b) Raman spectra of $V_{0.09}$–$Ni_{0.91}$MOF and Ni-MOF. c) TGA and DTG analysis of $V_{0.09}$–$Ni_{0.91}$MOF in N_2. d) N_2 adsorption-desorption isotherms with pore size distribution (inset) curves of $V_{0.09}$–$Ni_{0.91}$MOF, Ni-MOF and NiV–OH.

smaller nanoparticles, making it possible to have a higher specific surface area.

The presence of C, V, O, and Ni elements in $V_{0.09}$–$Ni_{0.91}$MOF and Ni-MOF was demonstrated in Figure S3. As shown in Figure 4a, the three peaks in the C 1s spectrum are calibrated as C=C (284.0 eV), C–O (286.0 eV) and –O–C=O (288.0 eV), respectively. In addition, the XPS spectra of all elements in the composite are corrected by the binding energy of C=C element

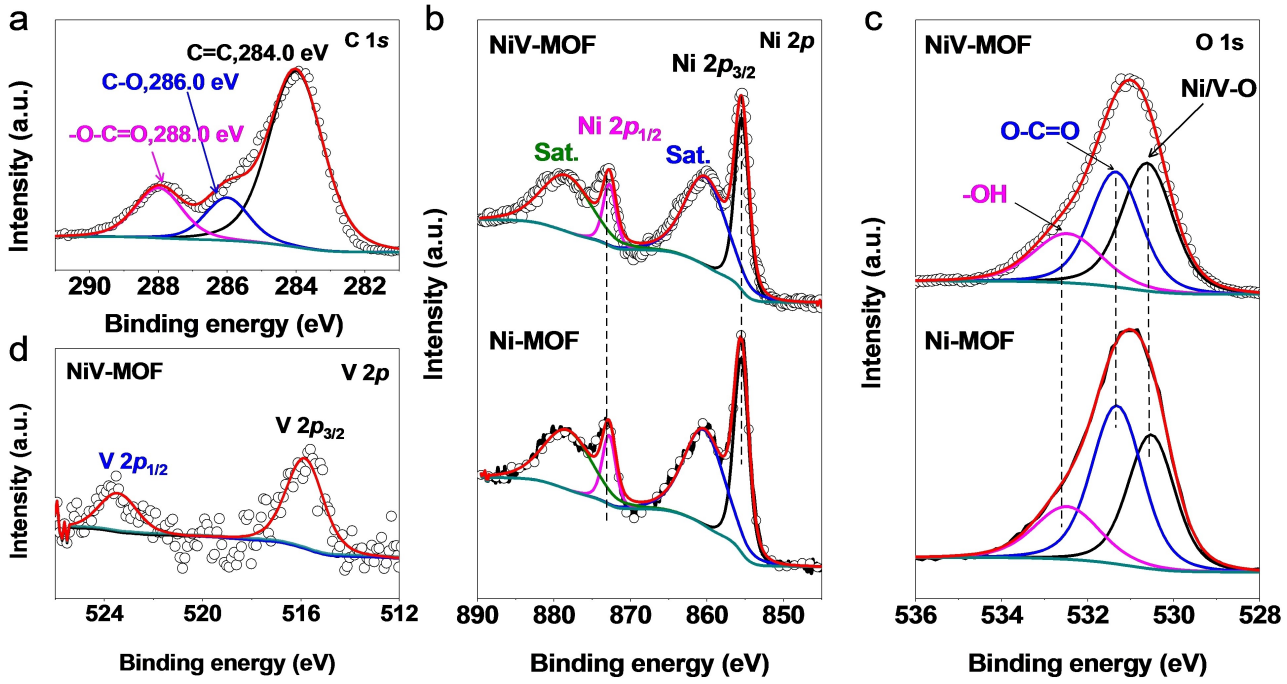

Figure 4. XPS spectra of a) C 1s and b) Ni 2p of $V_{0.09}$–$Ni_{0.91}$MOF and Ni-MOF, c) O 1s of $V_{0.09}$–$Ni_{0.91}$MOF and Ni-MOF, and d) V 2p of $V_{0.09}$–$Ni_{0.91}$MOF.

(284.0 eV). Two peaks at 873.5 and 856.2 eV in the Ni 2p spectrum (Figure 4b) were ascribed to Ni $2p_{1/2}$ and Ni $2p_{3/2}$ in $V_{0.09}$–$Ni_{0.91}$MOF and Ni-MOF, respectively,[19] and the other two satellite peaks were attributed to Ni^{2+} at 879.3 and 862.0 eV, respectively.[20] In the O 1s XPS spectrum of $V_{0.09}$–$Ni_{0.91}$MOF and Ni-MOF are displayed in Figure 4c. The peaks at 530.7 and 531.3 eV represent oxygen in metal oxides and oxygen in carboxylate group of ligand (DHTA), respectively.[21] Meanwhile, the binding energy at 532.3 eV is assigned to –OH from adsorbed H_2O molecule.[22] FTIR spectroscopy confirmed the presence of M–OH bonds, which reflected the interaction between Ni, V atoms and hydroxy groups (Figure 3a). As for V 2p (Figure 4d), the binding energies emerging at 516.3 and 523.9 eV correspond to V $2p_{3/2}$ and V $2p_{1/2}$, respectively, manifesting that V is doped in the $V_{0.09}$–$Ni_{0.91}$MOF with a +4 state.[23] According to the above XPS spectrum analysis, it can be further determined that the $V_{0.09}$–$Ni_{0.91}$MOF composite is formed. Due to the low content of introduced V, there is no significant effect on the chemical valence state of NiV-MOF.

The OER performance of a series of catalysts in 1 M KOH was assessed using a typical three-electrode configuration. The catalytic performance of V–Ni-MOF/NF was optimized in terms of total metal loading in Figure S5a. Figure 5a shows the linear sweep voltammetry (LSV) curve of the catalysts in alkaline solution after *iR* correction. The $V_{0.09}$–$Ni_{0.91}$MOF/NF shows the lowest overpotential of 235 mV at 10 mA cm^{-2} among all the precursors, including Ni-MOF/NF (278 mV), NiV-OH/NF (325 mV), NiV-MOF/NF (385 mV), and bare NF (385 mV), which is comparable to RuO_2/NF (230 mV). The overpotential of $V_{0.09}$–$Ni_{0.91}$MOF/NF was still the lowest except RuO_2/NF at high current density, indicating that the NiV-OH/NF improves the interaction between catalysts and NF support to improve the electrochemical performance permanently. In addition, the overpotentials of the catalysts at various current densities are summarized in Figure S4. More comfortingly, the Tafel slope is a crucial index for assessing the kinetic activity of OER in electrochemical process. In Figure 5b, the Tafel slope of $V_{0.09}$–$Ni_{0.91}$MOF (107 mV dec^{-1}) is the smallest in compared with NiV-OH/NF (133 mV dec^{-1}), NiV-MOF/NF (154 mV dec^{-1}), Ni-MOF/NF (115 mV dec^{-1}), RuO_2/NF (78 mV dec^{-1}), and bare NF (145 mV dec^{-1}). Meanwhile, the Tafel slope of $V_{0.09}$–$Ni_{0.91}$MOF/NF is the smallest among the three catalysts with different Ni/V ratios (Figure S5b), confirming $V_{0.09}$–$Ni_{0.91}$MOF/NF has the superior electrocatalytic activity and most effective catalytic kinetics for OER.[24] In addition, the η_{10} value and Tafel slope of $V_{0.09}$–$Ni_{0.91}$MOF/NF are also much lower than other phosphorus-containing OER catalysts recently reported in alkaline media (Figure 5c and Table S1). The electrochemical active surface areas of a series of catalysts were calculated according to double layer capacitance (C_{dl}) in the non-Faradaic region to evaluate their catalytic activity (Figure S6).[25] As showed in Figures 5d and S5c, d, $V_{0.09}$–$Ni_{0.91}$MOF/NF shows a higher C_{dl} value (15.4 mF cm^{-2}) due to its larger specific surface area and ultrathin mesoporous nanostructure, which provides more active sites to promote charge/mass transfer during OER.[26] Besides, the TOF value estimates the intrinsic catalytic activity

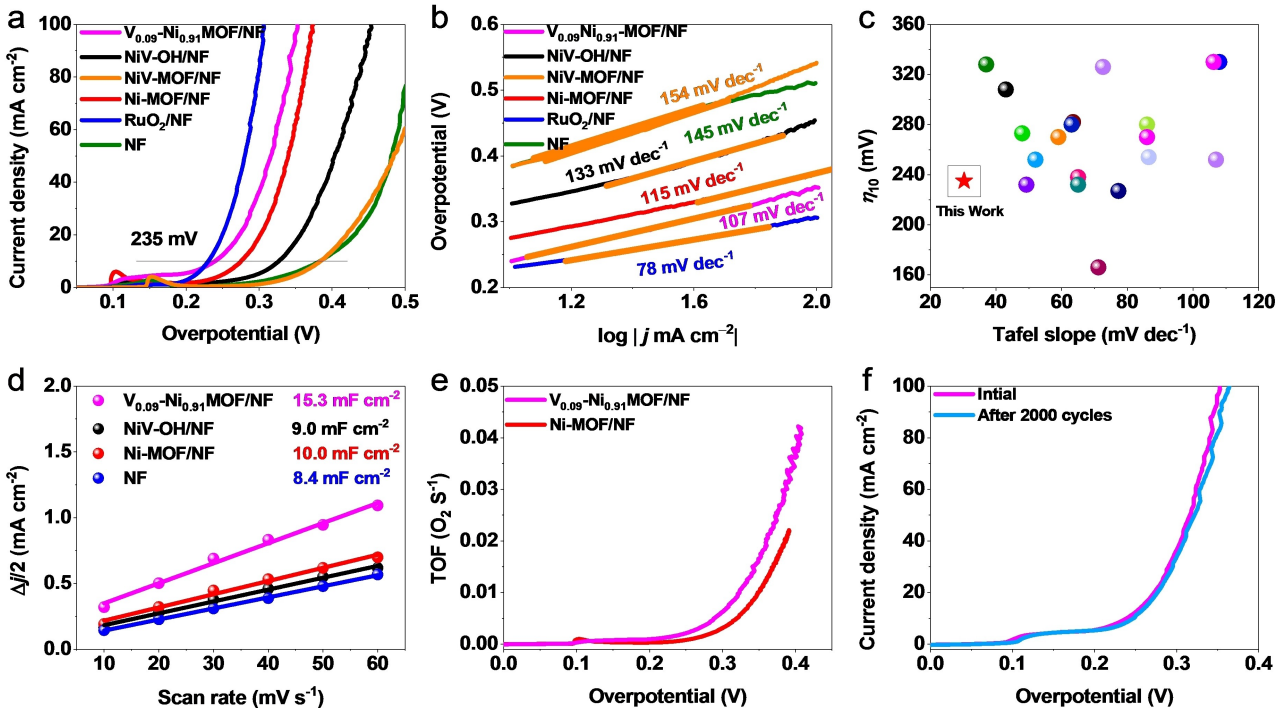

Figure 5. a) Linear sweep voltammetry (LSV) curves of $V_{0.09}$–$Ni_{0.91}$MOF/NF, NiV-OH/NF, Ni-MOF/NF, RuO_2/NF and bare NF with a scan rate of 0.5 mV– s^{-1}. b) Corresponding Tafel plots. c) Compared with the recently reported OER catalysts at overpotential of 10 mA cm^{-2} and Tafel slope. d) C_{dl} calculations. e) Turnover frequency (TOF) profiles versus overpotential of $V_{0.09}$–$Ni_{0.91}$MOF/NF and Ni-MOF/NF. f) Polarization curves of the initial and 2000th cycles of $V_{0.09}$–$Ni_{0.91}$MOF/NF.

of each active catalytic site.[27] Figures 5e and S7 shows TOF curves at various overpotentials derived using the metal content obtained by ICP. The TOF values of all catalysts exhibited a monotonic increase with increasing overpotential. Among all other catalysts, the $V_{0.09}$–$Ni_{0.91}$MOF/NF exhibits the highest intrinsic catalytic activity at the same overpotential suggesting the best OER performance.[28] After 2000 cycles, the LSV curve of $V_{0.09}$–$Ni_{0.91}$MOF/NF showed a slight loss of activity (Figure 5f). The electrochemical impedance spectroscopy (EIS) of $V_{0.09}$–$Ni_{0.91}$MOF/NF showed a higher electrical conductivity. Its R_{ct} value (1.1 Ω) is lower than that of $Ni_{0.16}Ni_{0.84}$-MOF/NF (1.8 Ω), $Ni_{0.02}Ni_{0.98}$-MOF/NF (2.0 Ω), NiV-OH/NF (3.3 Ω), Ni-MOF/NF (3.6 Ω), RuO_2 (1.5 Ω) and NF (6.8 Ω) (Figure S8). The small transfer resistance supports better OER performance.[29] Furthermore, the long-term durability of $V_{0.09}$–$Ni_{0.91}$MOF/NF was evaluated at 10 mA cm^{-2} as shown in Figure S9. The result indicated excellent stability after 72 h with an insignificant loss in activity. Additionally, the HER performance of $V_{0.09}$–$Ni_{0.91}$MOF/NF was also performed, which exhibited a poor overpotential of 187 mV at a current density of 10 mA cm^{-2} (Figure S10).

Therefore, the overall water splitting device was assembled using Pt/C/NF and $V_{0.09}$–$Ni_{0.91}$MOF/NF as cathode and anode in 30 wt.% KOH, respectively (Figure 6a). Figure 6b illustrates that the two-electrode device can drive a current density of 100 mA cm^{-2} with a very low cell voltage of 1.61 V. When the current density is approximately 343 mA cm^{-2}, the $V_{0.09}$–$Ni_{0.91}$MOF/NF$^{(+)}$||Pt/C/NF$^{(-)}$ and RuO_2/NF$^{(+)}$||Pt/C/NF$^{(-)}$ to the same voltage value. It is worth noting that $V_{0.09}$–$Ni_{0.91}$MOF/NF$^{(+)}$||Pt/C/NF$^{(-)}$ is always far superior to $V_{0.09}$–$Ni_{0.91}$MOF/NF$^{(+)}$||$V_{0.09}$–$Ni_{0.91}$MOF/NF$^{(-)}$. Furthermore, it surpasses noble metal and other recently reported bifunctional electrocatalysts after the critical point at 343 mA cm^{-2} (Figure 6c and Table S2). Meanwhile, $V_{0.09}$–$Ni_{0.91}$MOF/NF$^{(+)}$||Pt/C/NF$^{(-)}$ still maintains 92.7% activity after 80 h of continuous operation at a current density of 400 mA cm^{-2} (Figure 6d), suggesting a promising industrial perspective.

A series of characterizations were performed to investigate the composition changes of $V_{0.09}$–$Ni_{0.91}$MOF/NF after OER. The XRD of $V_{0.09}$–$Ni_{0.91}$MOF/NF after the OER stability test was consistent with $Ni(OH)_2$ (JCPDS: 14-0117) and NiOOH (JCPDS: 06-0075), indicating that the NiOOH and part of $Ni(OH)_2$ were formed during the OER process (Figure 7a). In-situ Raman tests were performed to further explore the mechanism of the actual catalytic species in the OER process.[30] At potentials below 1.35 V, the Raman spectra (Figure 7b, c) did not change significantly compared with the pristine $V_{0.09}$–$Ni_{0.91}$MOF/NF. At 1.40 V, the peaks at 479 and 555 cm^{-1} in the Raman spectrum might assigned to the bending vibration mode and A_{1g} stretching vibration mode of Ni–O in NiOOH, respectively, which are consistent with the oxidation peaks (100–200 mV) observed in the LSV curve (Figure 5a).[31] Interestingly, the tensile strength of the NiOOH peak starts to increase with increasing applied potential.

As displayed in Figure S11a, apart from the metal-oxygen bond vibrations, the stretching and deformation vibrations of the benzene ring and $\nu(COO^-)$ disappeared in the Raman

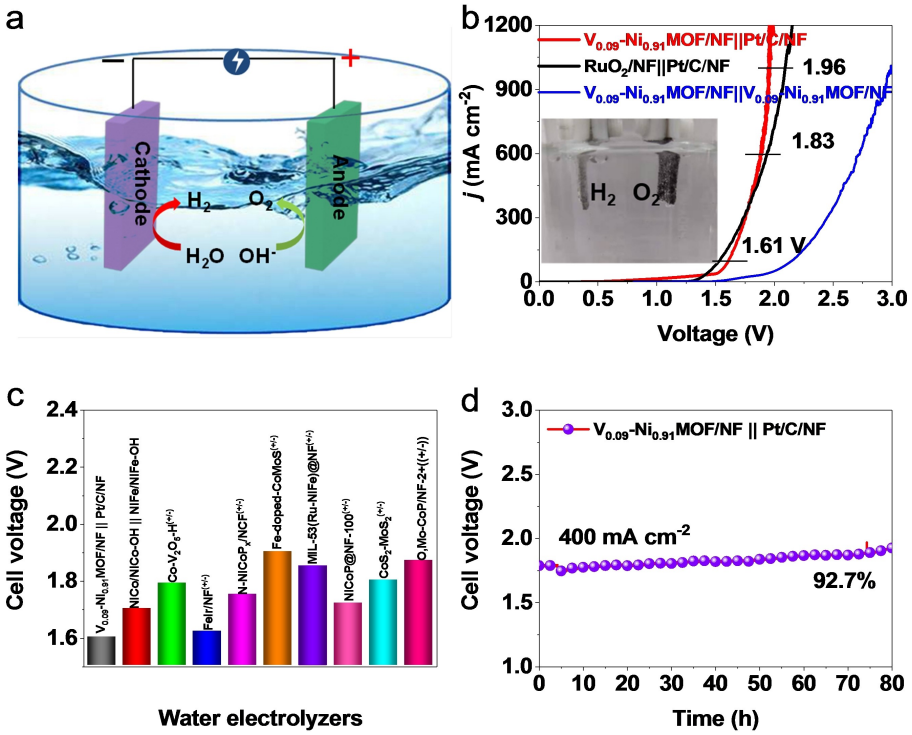

Figure 6. a) Schematic of the two-electrode system for overall water splitting with $V_{0.09}$–$Ni_{0.91}$MOF/NF as the anode and Pt/C/NF as the cathode. b) Overall water splitting polarization curves of $V_{0.09}$–$Ni_{0.91}$MOF/NF$^{(+)}$||Pt/C/NF$^{(-)}$, $V_{0.09}$–$Ni_{0.91}$MOF/NF$^{(+)}$||$V_{0.09}$–$Ni_{0.91}$MOF/NF$^{(-)}$ and RuO_2/NF$^{(+)}$||Pt/C/NF$^{(-)}$ in 30 wt% KOH. c) Comparing the cell voltage of the currently available electrolytic cell at 100 mA cm^{-2}. d) Stability of the $V_{0.09}$–$Ni_{0.91}$MOF/NF$^{(+)}$||Pt/C/NF$^{(-)}$ at 400 mA cm^{-2} for overall water splitting.

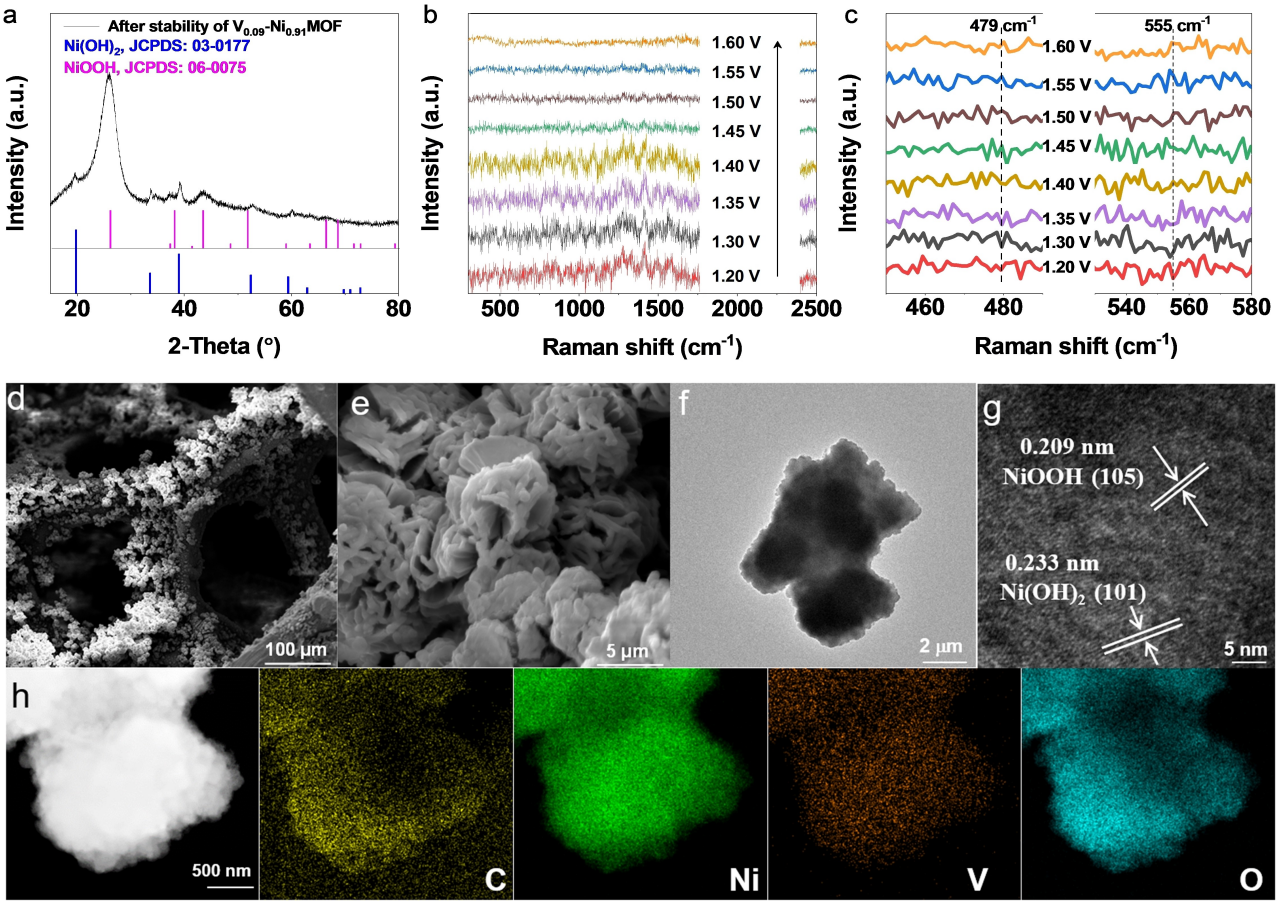

Figure 7. a) XRD pattern of $V_{0.09}$–$Ni_{0.91}$MOF after stability. In-situ Raman spectra with different ranges of b) 300–1800 cm^{-1}, c) 450–490 cm^{-1}, and 530–580 cm^{-1} of a $V_{0.09}$–$Ni_{0.91}$MOF/NF electrode at different potentials ranging from 1.20 to 1.60 V. d), e) SEM images, f) TEM image, g) HRTEM image, and h) HAADF-STEM image and the corresponding element mappings of $V_{0.09}$–$Ni_{0.91}$MOF/NF after an OER stability test.

spectra after the stability test. FTIR spectra showed that $V_{0.09}$–$Ni_{0.91}$MOF/NF had similar COO^- and OH^- to DHTA ligands after stability test, indicating free ligands' existence after dissociation of NiV-MOF structure (Figure S11b).[32] The SEM images showed that the morphology of the catalyst was partially agglomerated after stabilization (Figure 7d, e). The TEM image is consistent with the SEM results (Figure 7f). The well-resolved lattice fringes in HRTEM is 0.209 and 0.233 nm, corresponding to the (105) plane of NiOOH and the (101) plane of $Ni(OH)_2$ (Figure 7g). In addition, the HAADF-STEM image and corresponding elemental mappings reveal that C, Ni, V and O elements are uniformly distributed after OER stability test (Figure 7h). Furthermore, the XPS analysis of $V_{0.09}$–$Ni_{0.91}$MOF/NF before and after the OER is presented in Figures S12 and S13. After the stability test, the metallic Ni content increased while the V content decreased slightly, which may be attributed to the V leaching to accommodate the structural transformation.[13b] The prominent peaks of O 1s after the OER at 530.7, 531.3 and 532.3 eV can be deconvoluted into the typical M–O in NiOOH, oxygen in the ligand carboxylate (DHTA), and –OH in the adsorbed H_2O molecule, respectively.[33] Therefore, the combination of XRD, FTIR spectra, Raman spectra, HRTEM, XPS and in-situ Raman analysis indicated that the NiOOH is likely the actual catalytically active site in the OER process.[34]

As previously stated, the exceptional OER activity with remarkable durability of $V_{0.09}$–$Ni_{0.91}$MOF/NF in the alkaline electrolyte can be attributed to the following points: I) The self-supporting binder-free electrode prepared through the hydrothermal method can reduce the electrode resistance and accelerate electron transport during electrocatalysis.[22c,35] II) The spherical structure with a three-dimensional open framework facilitates electrolyte diffusion and gas emission.[36] III) The $V_{0.09}$–$Ni_{0.91}$MOF formed after V doping has a larger specific surface area, providing more efficient catalytic active sites for the OER process.[37] IV) The composite catalyst formed by V doping is beneficial in adjusting the binding energy between the active site and the intermediate, thereby enhancing the OER catalytic activity.[38]

Conclusion

In summary, we have designed a facile two-pot solvothermal method to synthesize the $V_{0.09}$–$Ni_{0.91}$MOF electrocatalyst for the OER and assemble a two-electrode system for water splitting.

The findings reveal that V doping can elevate Ni-MOF reaction kinetics and charge transfer efficiency substantially. As a result, $V_{0.09}$–$Ni_{0.91}$MOF demonstrated remarkable oxygen evolution performance, delivering 10 mA cm^{-2} with the lowest overpotential of 235 mV. Interestingly, the optimized catalyst outperformed the commonly used noble metal catalyst (RuO_2/NF) at high current density, thus indicating a broader application perspective. More importantly, the overall water splitting was constructed with Pt/C/NF and $V_{0.09}$–$Ni_{0.91}$MOF electrodes as cathode and anode, respectively, with a cell voltage of only 1.93 V at a current density of 1000 mA cm^{-2}. The excellent catalytic activity is mainly attributed to the unique three-dimensional self-supported structure, which provides more active sites, faster charge transfer characteristics, and synergies between different components to optimize the binding energy of OER intermediates.

Experimental Section

Synthesis of NiV-OH on NF: The typical synthesis procedure is described as follows. NF (1.5 cm × 2.5 cm) was ultrasonically cleaned with 1.0 M HCl, ethanol and deionized water for 10 min to remove impurities and oxides on the surface. 2.5 mmol $Ni(NO_3)_2 \cdot 6H_2O$, 0.25 mmol NH_4VO_3, 6.0 mmol $CO(NH_2)_2$ and 2 mmol NH_4F were dissolved in 30 mL deionized water and then sonicated for 30 min to obtain a clear solution. Then, the mixture was transferred to a Teflon-lined stainless-steel autoclave (50 mL) with a clean NF (1.5 cm × 2.5 cm), and heated to 120 °C and kept for 6 h. After cooling to room temperature, the obtained NiV-OH/NF was washed with deionized water 3 times, and then dried in an oven at 70 °C for 2 h.

Synthesis of $V_{1-x}Ni_xMOF/NF$: Firstly, 2.5 mmol $Ni(NO_3)_2 \cdot 6H_2O$, 0.25 mmol NH_4VO_3, and 1.5 mmol 2,5-dihydroxyterephthalic acid (DHTA) were dissolved in the mixed solution of 28 mL DMF, 2 mL ethanol, and 2 mL deionized water, and sonicated for 30 min to form a homogeneous solution. Secondly, the mixture of solution and NiV-OH/NF were transferred to Teflon-lined stainless-steel autoclave and maintained at 120 °C for 12 h. After cooling to room temperature, the obtained $V_{0.09}$–$Ni_{0.91}$MOF/NF was washed with deionized water for 3 times, and dried at 60 °C for 2 h. The loading of the composite was ~10.4 mg cm^{-2}.

As a comparison, the composite materials with different molar ratios of Ni and V were synthesized at 1.00/0.00, 0.84/0.16 and 0.98/0.02 under the same total metal molar and similar synthesis methods. The constructed materials were nominated as Ni-MOF/NF, $V_{0.16}$–$Ni_{0.84}$MOF/NF, and $V_{0.02}$–$Ni_{0.98}$MOF/NF.

Synthesis of NiV-MOF/NF: Firstly, 2.5 mmol $Ni(NO_3)_2 \cdot 6H_2O$, 0.25 mmol NH_4VO_3, and 1.5 mmol 2,5-dihydroxyterephthalic acid (DHTA) were dissolved in the mixed solution of 28 mL DMF, 2 mL ethanol, and 2 mL deionized water, and sonicated for 30 min to form a homogeneous solution. Secondly, the mixed solution and a piece of pure NF were transferred to Teflon-lined stainless-steel autoclave and maintained at 120 °C for 12 h. After cooling to room temperature, the obtained NiV-MOF/NF was washed with deionized water for 3 times, and dried at 60 °C for 2 h.

Preparation of RuO_2/NF and Pt/C/NF electrode: A mixed solution was formed by dispersing 5.0 mg of RuO_2 powder or commercial Pt/C (Johnson-Matthey) in 490 μL of deionized water, 490 μL of absolute ethanol, and 20 μL 5% Nafion. After ultrasonic treatment for 30 min, 200 μL of the solution was pipetted onto a NF (1 cm × 1 cm) and dried at room temperature for further use.

Acknowledgements

This work was supported by the National Natural Science Foundation of China (no. 21965005), Natural Science Foundation of Guangxi Province (2018GXNSFAA294077 and 2021GXNSFAA076001), Project of High-Level Talents of Guangxi (F-KA18015), and Guangxi Technology Base and Talent Subject (GUIKE AD18126001 and GUIKE AD20297039).

Conflict of Interest

The authors declare that they have no known competing financial interests or personal relationships that could have influenced the work reported in this paper.

Data Availability Statement

Research data are not shared.

Keywords: electrocatalysis · ion doping · metal-organic frameworks · oxygen evolution reaction · overall water splitting

[1] a) V. H. Hoa, D. T. Tran, D. C. Nguyen, D. H. Kim, N. H. Kim, J. H. Lee, *Adv. Funct. Mater.* **2020**, *30*, 2002533; b) J. Xiang, J. Li, X. Yang, S. Gao, R. Cao, *Acta Phys. Chim. Sin.* **2022**, *38*, 2205039–2205030; c) Y. Liu, Y. Wang, B. Liu, M. Amer, K. Yan, *Acta Phys. Chim. Sin.* **2022**, *38*, 2205028–2205020.
[2] a) K. Zhu, J. Chen, W. Wang, J. Liao, J. Dong, M. O. L. Chee, N. Wang, P. Dong, P. M. Ajayan, S. Gao, J. Shen, M. Ye, *Adv. Funct. Mater.* **2020**, *30*, 2003556; b) Z. Kang, H. Guo, J. Wu, X. Sun, Z. Zhang, Q. Liao, S. Zhang, H. Si, P. Wu, L. Wang, Y. Zhang, *Adv. Funct. Mater.* **2019**, *29*, 1807031.
[3] a) N. T. Suen, S. F. Hung, Q. Quan, N. Zhang, Y. J. Xu, H. M. Chen, *Chem. Soc. Rev.* **2017**, *46*, 337–365; b) F. Lv, W. Zhang, W. Yang, J. Feng, K. Wang, J. Zhou, P. Zhou, S. Guo, *Small Methods* **2019**, *4*, 1900129.
[4] F. Gao, Y. Zhang, Z. Wu, H. You, Y. Du, *Coord. Chem. Rev.* **2021**, *436*, 213825.
[5] a) M. A. Khan, H. Zhao, W. Zou, Z. Chen, W. Cao, J. Fang, J. Xu, L. Zhang, J. Zhang, *Electrochem. Energy Rev.* **2018**, *1*, 483–530; b) Q. Peng, X. Shao, C. Hu, Z. Luo, T. Taylor Isimjan, Z. Dou, R. Hou, X. Yang, *J. Colloid Interface Sci.* **2022**, *615*, 577–586.
[6] a) W.-J. Jiang, T. Tang, Y. Zhang, J.-S. Hu, *Acc. Chem. Res.* **2020**, *53*, 1111–1123; b) L. Wang, Z. Huang, H. Huang, S. Zhong, M. Huang, T. T. Isimjan, X. Yang, *Electrochim. Acta* **2022**, *404*, 139598.
[7] Q. Chang, Y. Xu, Z. Duan, F. Xiao, F. Fu, Y. Hong, J. Kim, S. I. Choi, D. Su, M. Shao, *Nano Lett.* **2017**, *17*, 3926–3931.
[8] a) C. Wu, X. Zhang, H. Li, Z. Xia, S. Yu, S. Wang, G. Sun, *Chin. J. Catal.* **2021**, *42*, 637–647; b) S. Yu, Y. Wu, Q. Xue, J.-J. Zhu, Y. Zhou, *J. Mater. Chem. A* **2022**, *10*, 4936–4943; c) F. Gao, Y. Zhang, F. Ren, Y. Shiraishi, Y. Du, *Adv. Funct. Mater.* **2020**, *30*, 2000255.
[9] K. Ge, S. Sun, Y. Zhao, K. Yang, S. Wang, Z. Zhang, J. Cao, Y. Yang, Y. Zhang, M. Pan, L. Zhu, *Angew. Chem. Int. Ed.* **2021**, *60*, 12097–12102.
[10] W. Zhou, D.-D. Huang, Y.-P. Wu, J. Zhao, T. Wu, J. Zhang, D.-S. Li, C. Sun, P. Feng, X. Bu, *Angew. Chem. Int. Ed.* **2019**, *58*, 4227–4231; *Angew. Chem.* **2019**, *131*, 4271–4275.
[11] Y. Shi, Y. Yu, Y. Liang, Y. Du, B. Zhang, *Angew. Chem. Int. Ed.* **2019**, *58*, 3769–3773; *Angew. Chem.* **2019**, *131*, 3809–3813.
[12] a) Y. Wang, B. Liu, X. Shen, H. Arandiyan, T. Zhao, Y. Li, M. Garbrecht, Z. Su, L. Han, A. Tricoli, C. Zhao, *Adv. Energy Mater.* **2021**, *11*, 2003759; b) S. Du, C. Wu, L. Ao, X. Zhou, K. Jiang, L. Shang, Y. Li, J. Zhang, Z. Hu, J. Chu,

Chem. Eng. J. **2020**, *420*, 127714; c) S. Niu, W. J. Jiang, Z. Wei, T. Tang, J. Ma, J. S. Hu, L. J. Wan, *J. Am. Chem. Soc.* **2019**, *141*, 7005–7013.
[13] a) Z. Duan, X. Tan, Y. Sun, W.-c. Zhang, A. Umar, X. Wu, *ACS Appl. Nano Mater.* **2021**, *4*, 10791–10798; b) T. Zhao, X. Shen, Y. Wang, R. K. Hocking, Y. Li, C. Rong, K. Dastafkan, Z. Su, C. Zhao, *Adv. Funct. Mater.* **2021**, *31*, 2100614.
[14] L. Yang, G. Zhu, H. Wen, X. Guan, X. Sun, H. Feng, W. Tian, D. Zheng, X. Cheng, Y. Yao, *J. Mater. Chem. A* **2019**, *7*, 8771–8776.
[15] W. Peng, A. Deshmukh, N. Chen, Z. Lv, S. Zhao, J. Li, B. Yan, X. Gao, L. Shang, Y. Gong, L. Wu, M. Chen, T. Zhang, H. Gou, *ACS Catal.* **2022**, *12*, 3743–3751.
[16] Y. Qian, J. Yu, Y. Zhang, F. Zhang, Y. Kang, C. Su, H. Shi, D. J. Kang, H. Pang, *Small Methods* **2022**, *6*, 2101186.
[17] T. Udayabhaskararao, T. Altantzis, L. Houben, M. Coronado-Puchau, J. Langer, R. Popovitz-Biro, L. M. Liz-Marzán, L. Vuković, P. Král, S. Bals, R. Klajn, *Science* **2017**, *358*, 514–518.
[18] T. Udayabhaskararao, T. Altantzis, L. Houben, M. Coronado-Puchau, J. Langer, R. Popovitz-Biro, L. M. Liz-Marzan, L. Vukovic, P. Kral, S. Bals, R. Klajn, *Science* **2017**, *358*, 514–518.
[19] a) C. Yang, R. Zhao, H. Xiang, J. Wu, W. Zhong, W. Li, Q. Zhang, N. Yang, X. Li, *Adv. Energy Mater.* **2020**, *10*, 2002260; b) X. Ji, Y. Lin, J. Zeng, Z. Ren, Z. Lin, Y. Mu, Y. Qiu, J. Yu, *Nat. Commun.* **2021**, *12*, 1380.
[20] X. Luan, H. Du, Y. Kong, F. Qu, L. Lu, *Chem. Commun.* **2019**, *55*, 7335–7338.
[21] D. Liu, H. Xu, C. Wang, H. Shang, R. Yu, Y. Wang, J. Li, X. Li, Y. Du, *Inorg. Chem.* **2021**, *60*, 5882–5889.
[22] a) J. Li, W. Huang, M. Wang, S. Xi, J. Meng, K. Zhao, J. Jin, W. Xu, Z. Wang, X. Liu, Q. Chen, L. Xu, X. Liao, Y. Jiang, K. A. Owusu, B. Jiang, C. Chen, D. Fan, L. Zhou, L. Mai, *ACS Energy Lett.* **2018**, *4*, 285–292; b) Q. Zha, F. Yuan, G. Qin, Y. Ni, *Inorg. Chem.* **2020**, *59*, 1295–1305; c) L. Yin, X. Du, C. Di, M. Wang, K. Su, Z. Li, *Chem. Eng. J.* **2021**, *414*, 128809; d) C.-F. Li, L.-J. Xie, J.-W. Zhao, L.-F. Gu, H.-B. Tang, L. Zheng, G.-R. Li, *Angew. Chem. Int. Ed.* **2022**, *61*, e202116934.
[23] a) Y. Qu, M. Shao, Y. Shao, M. Yang, J. Xu, C. T. Kwok, X. Shi, Z. Lu, H. Pan, *J. Mater. Chem. A* **2017**, *5*, 15080–15086; b) L. An, J. Feng, Y. Zhang, R. Wang, H. Liu, G. C. Wang, F. Cheng, P. Xi, *Adv. Funct. Mater.* **2019**, *29*, 1805298.
[24] Q. Ji, Y. Kong, H. Tan, H. Duan, N. Li, B. Tang, Y. Wang, S. Feng, L. Lv, C. Wang, F. Hu, W. Zhang, L. Cai, W. Yan, *ACS Catal.* **2022**, *12*, 4318–4326.
[25] X.-J. Bai, H. Chen, Y.-N. Li, L. Shao, J.-C. Ma, L.-L. Li, J.-Y. Chen, T.-Q. Wang, X.-M. Zhang, L.-Y. Zhang, Y. Fu, W. Qi, *New J. Chem.* **2020**, *44*, 1694–1698.
[26] M. Ahn, I. Y. Cha, J. Cho, H. C. Ham, Y.-E. Sung, S. J. Yoo, *ACS Catal.* **2017**, *7*, 5796–5801.
[27] D. Chinnadurai, R. Rajendiran, O. L. Li, K. Prabakar, *App. Catal. B: Environ.* **2021**, *292*, 120202.
[28] Z. Wan, Q. He, Y. Qu, J. Dong, E. Shoko, P. Yan, T. Taylor Isimjan, X. Yang, *J. Electroanal. Chem.* **2022**, *904*, 115928.
[29] a) M. Arif, G. Yasin, L. Luo, W. Ye, M. A. Mushtaq, X. Fang, X. Xiang, S. Ji, D. Yan, *App. Catal. B: Environ.* **2020**, *265*, 118559; b) S. K. Ramesh, V. Ganesan, J. Kim, *ACS Appl. Energ. Mater.* **2021**, *4*, 12998–13005; c) X. Li, M. Fan, D. Wei, M. Li, Y. Wang, *Electrochim. Acta* **2020**, *354*, 136682; d) Y. Hu, Z. Luo, M. Guo, J. Dong, P. Yan, C. Hu, T. T. Isimjan, X. Yang, *Chem. Eng. J.* **2022**, *435*, 134795; e) Q. Peng, Q. He, Y. Hu, T. T. Isimjan, R. Hou, X. Yang, *J. Energy Chem.* **2022**, *65*, 574–582.
[30] D. Lan, Y. Rong, Y. Hou, Y. Yan, Z. Yu, L. Tu, S. Chen, J. Wei, Z. Li, *Sci. Total Environ.* **2022**, *805*, 150340.
[31] S. Zhao, C. Tan, C.-T. He, P. An, F. Xie, S. Jiang, Y. Zhu, K.-H. Wu, B. Zhang, H. Li, J. Zhang, Y. Chen, S. Liu, J. Dong, Z. Tang, *Nat. Energy* **2020**, *5*, 881–890.
[32] F. Sun, G. Wang, Y. Ding, C. Wang, B. Yuan, Y. Lin, *Adv. Energy Mater.* **2018**, *8*, 1800584.
[33] Q. Qian, Y. Li, Y. Liu, L. Yu, G. Zhang, *Adv. Mater.* **2019**, *31*, 1901139.
[34] a) D. Lv, S. Su, S. Zhang, D. Cai, *J. Alloys Compd.* **2022**, *912*, 165143; b) H. Sun, X. Xu, Z. Yan, X. Chen, F. Cheng, P. S. Weiss, J. Chen, *Chem. Mater.* **2017**, *29*, 8539–8547.
[35] Y. Wang, G. Qian, Q. Xu, H. Zhang, F. Shen, L. Luo, S. Yin, *Appl. Catal. B* **2021**, *286*, 119881.
[36] Y. Zhang, Z. Li, K. Zhang, Z. Wu, F. Gao, Y. Du, *Appl. Surf. Sci.* **2022**, *590*, 153102.
[37] L. Yang, H. Li, Y. Yu, Y. Wu, L. Zhang, *Appl. Catal. B* **2020**, *271*, 118939.
[38] a) Y. Cui, Y. Xue, R. Zhang, J. Zhang, X. a. Li, X. Zhu, *J. Mater. Chem. A* **2019**, *7*, 21911–21917; b) Y. Jeung, H. Jung, D. Kim, H. Roh, C. Lim, J. W. Han, K. Yong, *J. Mater. Chem. A* **2021**, *9*, 12203–12213; c) P. Zhou, X. Lv, D. Xing, F. Ma, Y. Liu, Z. Wang, P. Wang, Z. Zheng, Y. Dai, B. Huang, *Appl. Catal. B: Environ.* **2020**, *263*, 118330.

Manuscript received: June 10, 2022
Accepted manuscript online: August 7, 2022
Version of record online: August 31, 2022